npj | climate and atmospheric science

Article

Published in partnership with CECCR at King Abdulaziz University

https://doi.org/10.1038/s41612-025-01316-1

Modulation of tropical cyclone intensity by current–wind interaction

Ajin Cho[1], Hajoon Song[1,2] ✉, Il-Ju Moon[3], Hyodae Seo[4], Rui Sun[5], Matthew R. Mazloff[5], Aneesh C. Subramanian[6], Bruce D. Cornuelle[5] & Arthur J. Miller[5]

Current–wind interaction modulates air–sea momentum and turbulent heat fluxes, which are critical in the energy cycle of tropical cyclones (TCs). However, the effects of the surface currents on air–sea exchange under TCs have remained unclear. Here, using an atmosphere–ocean coupled model, we investigate the role of current–wind interaction in determining TC intensity. Surface currents generally align with surface winds. Accounting for the current–wind interaction, the alignment reduces both the air–sea turbulent heat flux and momentum flux (average 1.0% and 2.5%), which serve as the energy source and sink of TCs, respectively. The reduction in the energy source (sink) decreases (increases) the TC growth −1.9% (+1.3%) on average and up to −13.7% (+11.1%). For simulations extending beyond the seasonal scale, the accumulated impacts of current–wind interaction alter TC genesis, affecting surface wind speed and sea surface temperature during the TC season. These findings reveal an important feedback mechanism associated with TCs driven by the current–wind interaction.

The atmosphere and ocean, two major components of the climate system, exchange momentum, heat, moisture, and other properties, which are represented as air–sea fluxes. Air–sea fluxes play a crucial role in the occurrence and development of atmospheric circulation patterns and extreme phenomena, and in numerical models that predict weather and climate[1,2]. As the energy exchange differs depending on the state of the interface, it is necessary to further investigate the representation of air–sea fluxes and the associated atmospheric and oceanic responses[3,4].

In recent years, the role of surface currents in modifying air–sea fluxes, particularly through current–wind interaction, has garnered increasing attention. Numerous studies have demonstrated that calculating wind stress using wind velocity relative to the ocean current (relative wind, RW) rather than the absolute wind (AW) results in reduced wind work, which in turn dampens mesoscale oceanic kinetic energy and slows the mean flow[5–12]. This effect, also known as either the RW effect or current feedback effect, underscores the influence of ocean currents on air–sea momentum exchange.

In addition to air–sea momentum flux, the current–wind interaction also impacts heat and moisture fluxes[13]. In particular, when surface currents are strong and aligned with the wind directions, heat and moisture fluxes calculated with RW can be substantially lower than those with AW. In some cases, this effect is as significant as that on momentum flux, even altering surface current structures in the Kuroshio Extension[13]. These findings imply that since ocean currents represent the motion of the air–sea interface itself, they can affect all components of the air–sea flux and potentially feed back into the ocean state.

Although previous works have advanced our understanding of current–wind interactions, including their effects on flux modifications and ocean energetics under various atmospheric regimes, it remains unclear whether current–wind interaction can produce meaningful atmospheric responses under extreme wind conditions, such as within tropical cyclones (TCs). TCs gain energy from heat supplied at the sea surface, and the resulting strong winds generate intense wind stress, which, in turn, impacts the ocean[14,15].

Research on TC–ocean interactions has been conducted from multiple perspectives. For instance, there are studies focusing on the oceanic responses to TCs, particularly the ocean mixing-driven cooling of sea surface temperatures (SSTs), a process known as a cold wake[16–19]. Many studies have investigated how cold wakes and ocean stratification influence TC evolution[20,21], while others have examined the role of ocean surface waves in modulating air–sea momentum and heat fluxes[22–24]. However, the impact of TC-induced surface current on TC intensity has remained unexplored.

[1]Department of Atmospheric Sciences, Yonsei University, 50 Yonsei-ro, Seodaemun-gu, 03722 Seoul, Republic of Korea. [2]Division of Environmental Science & Engineering, Pohang University of Science and Technology, 77 Cheonam-ro, Pohang-si, 37673 Gyeongsangbuk-do, Republic of Korea. [3]Typhoon Research Center, Jeju National University, 102 Jejudaehak-ro, Jeju-si, 63243 Jeju Special Self-Governing Province, Republic of Korea. [4]Department of Oceanography, University of Hawai'i at Mānoa, 2500 Campus Road, Honolulu, 96822 HI, USA. [5]Scripps Institution of Oceanography, University of California, San Diego, 9500 Gilman Drive, La Jolla, 92093 CA, USA. [6]Department of Atmospheric and Oceanic Sciences, University of Colorado Boulder, 4001 Discovery Drive, Boulder, 80303 CO, USA. ✉e-mail: hajsong@yonsei.ac.kr

Table 1 | Experimental cases in the present work

Case name	Formulation
AW	Wind stress: $\rho_a C_D \lvert\mathbf{V}_{atm}\rvert \mathbf{V}_{atm}$
	Enthalpy flux: $\rho_a C_h (h^* - h) \lvert\mathbf{V}_{atm}\rvert$
RW_τ	Wind stress: $\rho_a C_D \lvert\mathbf{V}_{atm} - \mathbf{V}_{ocn}\rvert (\mathbf{V}_{atm} - \mathbf{V}_{ocn})$
	Enthalpy flux: $\rho_a C_h (h^* - h) \lvert\mathbf{V}_{atm}\rvert$
RW_Q	Wind stress: $\rho_a C_D \lvert\mathbf{V}_{atm}\rvert \mathbf{V}_{atm}$
	Enthalpy flux: $\rho_a C_h (h^* - h) \lvert\mathbf{V}_{atm} - \mathbf{V}_{ocn}\rvert$
RW_{both}	Wind stress: $\rho_a C_D \lvert\mathbf{V}_{atm} - \mathbf{V}_{ocn}\rvert (\mathbf{V}_{atm} - \mathbf{V}_{ocn})$
	Enthalpy flux: $\rho_a C_h (h^* - h) \lvert\mathbf{V}_{atm} - \mathbf{V}_{ocn}\rvert$

C_h and C_D are the exchange coefficients for enthalpy and momentum, respectively, $\mathbf{V}_{atm}$ and $\mathbf{V}_{ocn}$ are the surface wind and surface current vectors, h^* is the saturation enthalpy of the sea surface, and h is the enthalpy of atmosphere

Therefore, this study aims to address two main questions: (1) Can surface currents influence air–sea momentum and turbulent heat fluxes even under the extreme wind conditions of TCs? (2) If so, how do these flux changes affect TC intensity? Specifically, we examine the individual effects of current–wind interaction in air–sea momentum and turbulent heat fluxes, respectively, as well as the combined responses when both effects are included.

Results

Theoretical framework

TCs form over warm oceans, where temperatures exceed 26–27 °C[25]. They develop and move poleward, causing significant damage upon landfall due to strong winds and heavy rainfall[26]. Previously, numerous studies have been conducted to predict TC intensity in an effort to mitigate the potential damage. One approach is to predict TC intensity using the maximum potential intensity (PI) theory[14,27–29]. This theory estimates the TC's maximum surface wind speed after treating a mature TC as a Carnot heat engine where moist entropy is conserved. Several studies have modified the PI formula to incorporate the role of the upper ocean and changes in exchange coefficients under extreme wind conditions[30–33].

The PI formula, however, does not account for surface currents. Strong surface currents are generated beneath the TCs and tend to align with the winds most notably in the right (left) side of the TC track in Northern (Southern) Hemisphere[34,35]. These strong currents, 2–4% of the wind speeds, cause the magnitude—and to a lesser extent, the direction—of the relative wind vector to differ from those of the absolute wind vector. Accounting for surface currents alters the calculation of wind stress and enthalpy flux (latent plus sensible heat flux), and consequently, the PI of TCs as:

$$\begin{aligned} PI(RW_\tau) &= \tfrac{1}{\alpha^2 \cos\theta} PI(AW), \\ PI(RW_Q) &= \alpha PI(AW), \\ PI(RW_{both}) &= \tfrac{1}{\alpha \cos\theta} PI(AW) \end{aligned} \quad (1)$$

where AW, RW_τ, RW_Q and RW_{both} are the cases using different calculations of wind stress and enthalpy flux described in Table 1, α and θ are the ratio of the relative wind speed to the absolute wind speed and the angle between these two wind vectors, respectively. The derivation process is presented in the "Methods" section.

When the surface current vector and surface wind vector point in a similar direction, the scaling factor α becomes <1. In addition, since the surface current speed is much smaller than the surface wind speed under TCs, $\cos\theta$ remains between 0 and 1. Under this condition, both $PI(RW_\tau)$ and $PI(RW_{both})$ are greater than PI(AW), suggesting that neglecting surface currents may lead to an underestimation of TC intensity. It is noted that θ becomes irrelevant in the modification of PI when the surface currents are included in the turbulent heat flux. Additionally, the change in $PI(RW_{both})$ is consistently smaller than that in $PI(RW_\tau)$.

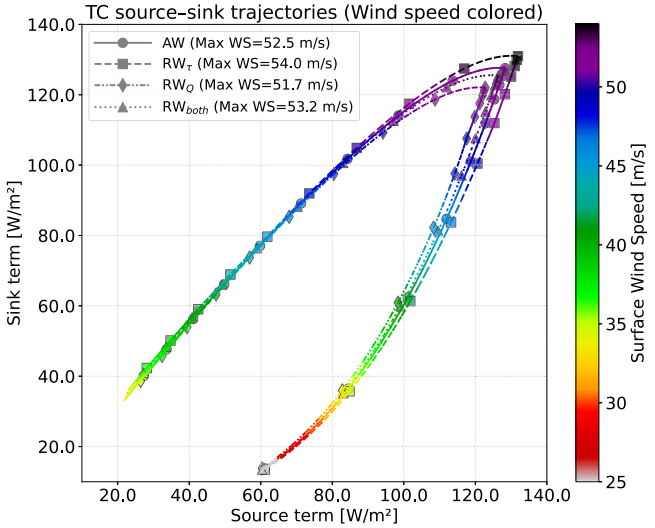

Fig. 1 | Changes in idealized TC surface wind speeds in source–sink space. x-axis denotes the source term (actual generation rate of mechanical energy) and the y-axis represents the sink term (dissipation rate of mechanical energy in the boundary layer). Each point corresponds to a time-dependent calculation (performed every 1 h), with color indicating the TC surface wind speed. For clarity, only every 12 h point is marked in the figure. Results from the control case (AW) and three sensitivity experiments are shown using different markers, illustrating how current–wind interactions modify the TC trajectory in the source–sink space.

While PI describes a steady-state intensity limit, real TCs undergo continuous development and decay. To assess how current–wind interaction influences TC energetics during transient phases, we compared the energy trajectories of the four cases listed in Table 1. From the rate of change of TC kinetic energy[36], we derive the growth rate of the TC wind speed for each case as follows:

$$\begin{aligned} \tfrac{d|\mathbf{V}_{atm}|}{dt}(\mathrm{AW}) &= \tfrac{1}{H|\mathbf{V}_{atm}|}\left(k\left(1-\tfrac{T_{out}}{T_s}\right)C_h(h^*-h)|\mathbf{V}_{atm}| - C_D\tfrac{T_{out}}{T_s}|\mathbf{V}_{atm}|^3\right), \\ \tfrac{d|\mathbf{V}_{atm}|}{dt}(\mathrm{RW}_\tau) &= \tfrac{1}{H|\mathbf{V}_{atm}|}(k\left(1-\tfrac{T_{out}}{T_s}\right)C_h(h^*-h)|\mathbf{V}_{atm}| \\ &\quad -C_D\tfrac{T_{out}}{T_s}|\mathbf{V}_{atm}-\mathbf{V}_{ocn}|^2|\mathbf{V}_{atm}|), \\ \tfrac{d|\mathbf{V}_{atm}|}{dt}(\mathrm{RW}_Q) &= \tfrac{1}{H|\mathbf{V}_{atm}|}(k\left(1-\tfrac{T_{out}}{T_s}\right)C_h(h^*-h)|\mathbf{V}_{atm}-\mathbf{V}_{ocn}| \\ &\quad -C_D\tfrac{T_{out}}{T_s}|\mathbf{V}_{atm}|^3), \\ \tfrac{d|\mathbf{V}_{atm}|}{dt}(\mathrm{RW}_{both}) &= \tfrac{1}{H|\mathbf{V}_{atm}|}(k\left(1-\tfrac{T_{out}}{T_s}\right)C_h(h^*-h)|\mathbf{V}_{atm}-\mathbf{V}_{ocn}| \\ &\quad -C_D\tfrac{T_{out}}{T_s}|\mathbf{V}_{atm}-\mathbf{V}_{ocn}|^2|\mathbf{V}_{atm}|) \end{aligned} \quad (2)$$

where T_s is the surface temperature, T_{out} is the temperature at the outflow layer, $H = \frac{1}{\rho}\int \rho(z)dz$ is the density scale height of the atmosphere and k is the relative efficiency factor ($0 \le k \le 1$). In each equation, the first term in the parentheses corresponds to the energy source term from the upward enthalpy flux, while the second term denotes the sink term from viscous dissipation. If the source exceeds the sink, the TC wind speed intensifies; otherwise, it weakens. Detailed descriptions are in the "Methods" section.

Figure 1 illustrates the change of TC wind speeds in the TC energy source–sink space, based on the growth rate of TC wind speed. To visualize this, we prescribed time-varying surface current speed, SST, and relative humidity as described in the "Methods" section and Fig. S9a–c. In RW_Q, the reduced enthalpy flux compared to AW lowers the source term, shifting the trajectory leftward (x-axis) and leading to a lower maximum wind speed when the source equals the sink. In RW_τ, weaker wind stress reduces the sink term, pushing the trajectory downward along the y-axis initially. This change allows for faster development of surface wind speed and yields

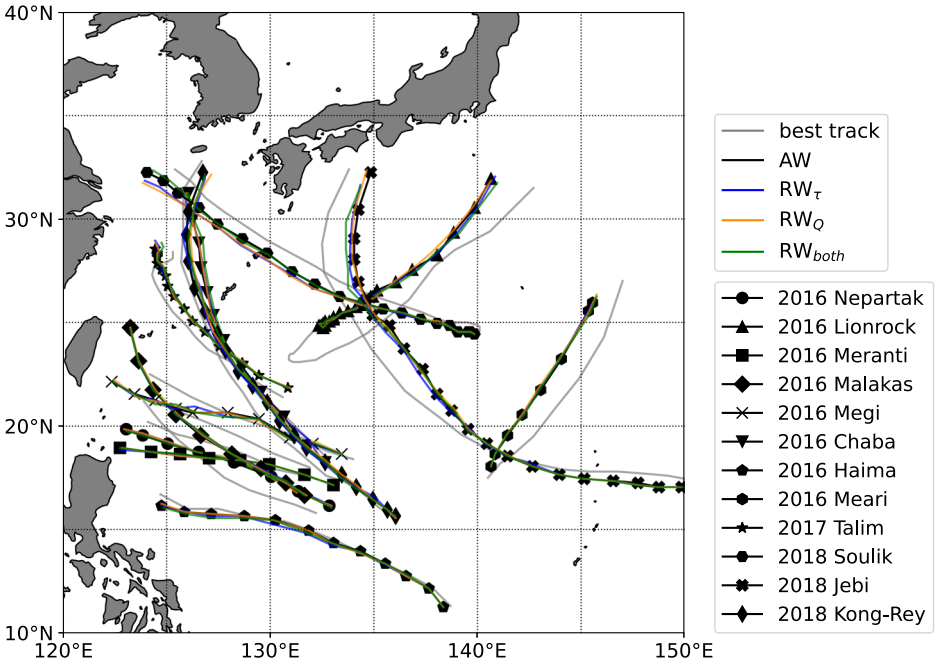

Fig. 2 | TC tracks in simulations and observations. The Joint Typhoon Warning Center (JTWC) best track and simulated tracks of TCs. Markers represent the location of minimum sea-level pressure every 6 h. Tracks are shown up to the point of landfall or dissipation, corresponding to the period used in the analysis. The colors represent the tracks from different experimental cases.

higher peak wind speed than AW. RW_{both} shows reductions in both source and sink terms, but the sink reduction dominates because the relative wind effect enters quadratically in the sink term (momentum flux) rather than linearly in the source term (heat flux). As a result, surface wind speeds exceed those in AW, despite the weakened source term.

These results demonstrate that surface currents modify the potential intensity and energy trajectory of TCs, thereby influencing their development. Based on this theoretical analysis, we evaluated how current–wind interactions influence TC intensity and the growth rate. The following subsection describes our numerical experiments, which aim to assess this theoretical framework.

Numerical simulations

To investigate whether current–wind interaction occurs under realistic TC conditions and how it affects TC intensity, we performed numerical simulations using a coupled atmosphere–ocean model. We designed four experimental cases (Table 1) and simulated twelve TCs that occurred in the western North Pacific from 2016−2018. The "Methods" section details the model configuration, TC selection processes and the criteria used for TC tracking. Figure 2 illustrates the simulated TC tracks along with the observed best tracks from the JTWC. Nudging was not applied in these simulations; therefore, the simulated tracks do not perfectly match the observations. However, the simulated cases exhibit similar tracks across four experimental cases. The individual TCs experience comparable environmental conditions, such as SST and atmospheric circulation, suggesting that changes in TC intensity are primarily due to the current–wind interaction rather than environmental factors. A comparison of the maximum wind speed with observations is provided in Fig. S1.

Some assumptions used in the theoretical framework do not fully apply to the simulated TCs. For instance, the PI theory assumes an axisymmetric TC structure isolated from external forces constraining its intensity. However, the simulated TCs are asymmetric and influenced by environmental conditions, such as vertical wind shear, which can suppress development. In addition, the theoretical diagram in Fig. 1 assumes that surface currents align with wind direction beneath the TC, which may not hold true in the simulations. Because the idealized assumptions are not strictly satisfied under more realistic TC conditions, this section aims to assess whether the impact of current–wind interaction persists in the numerical simulations.

TCs and surface currents

We first examine the characteristics of surface currents beneath the simulated TCs to assess their potential impact on air–sea fluxes. Figure 3a shows the average surface current speed and the wind–current angle (i.e., the angle between the surface wind and current vectors) under the TCs. Surface current speeds exceeded 0.4 m/s on average, and the wind–current angle was <50° on average with the exception near the left side of the TC track where wind and currents are strongly misaligned. Notably, the maximum current speeds exceeded 1 m/s on the right side of the TC's translation direction, and the associated wind–current angle was typically <40°. These results indicate that the consideration of surface currents under TCs leads to a reduction in air–sea fluxes, especially on the right side of the TCs where the current is more aligned with the wind.

To analyze the reduction of the relative wind speed relative to the absolute wind speed, we examined the ratio between the relative wind speed and the absolute wind speed (α). Figure 3b shows the distribution of α under the simulated TCs. Most values range between 0.925 and 1.025, with peaks around 0.98, indicating that the relative wind speeds are typically about 2% lower than the absolute wind speeds. When α is <1, the momentum flux calculated using the relative wind would be smaller by approximately the square of α, while the enthalpy fluxes would be smaller in direct proportion to α, compared with those using the absolute wind. We examined the mean value of α as a function of radius under the TCs. Choosing a smaller radius than 250 km may increase the wind stress and turbulent heat flux difference since the surface currents are strongest near the radius of maximum wind (RMW) which is around 70 km. However, since the maximum RMW of the analyzed TCs is around 175 km, we decide to use a larger radius to ensure inclusion of the strong surface current region. We also calculated the angle between those two wind vectors (θ in Eq. (1)). The mean θ across all TCs was within 2°, indicating the theoretical impact on intensity—expressed as $1/\cos\theta$—was <0.06%. These results suggest that changes in air–sea fluxes and TC intensity are primarily attributed to the difference in wind speed magnitude, represented by α. In our simulation, the thickness of the ocean model's top layer is 1 m; θ may be sensitive to this layer thickness[37], although the effect is expected to be small. Therefore, we focus on α in this section. In the next section, we examine whether this reduction leads to changes in air–sea fluxes and TC intensity, similar to the results in the Theoretical framework.

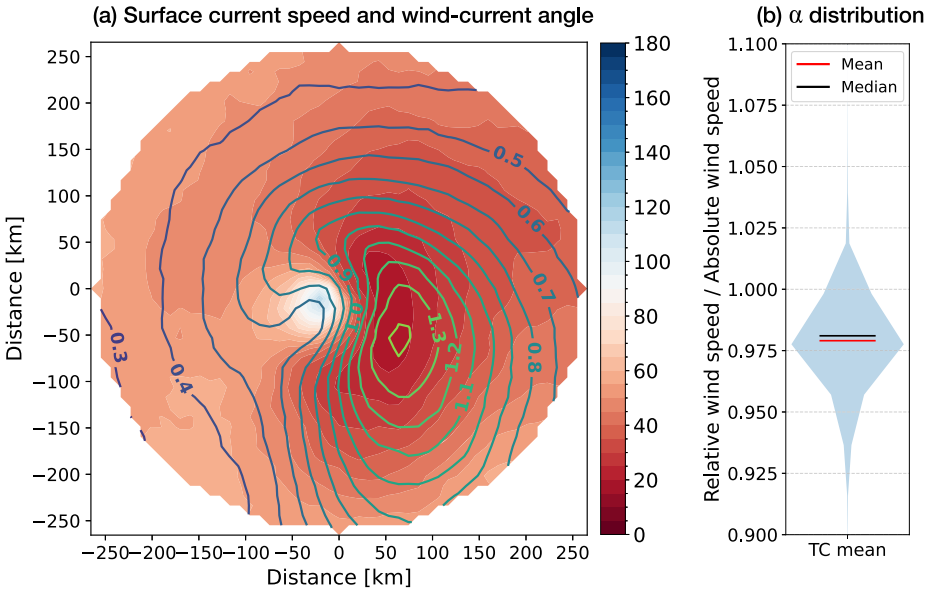

Fig. 3 | Surface current characteristics and relative wind speed under TCs. a Composite patterns of average surface current speed (contour) [m/s] and the angle between the surface wind and surface current (shading) [degrees] during the pre-landfall period of TCs in the AW experimental case, within a 250 km radius from the TC center, defined as the location of minimum surface pressure. The patterns are shown by following the TCs with the y-axis aligned to the TC's moving direction with 6-hourly simulation data. **b** Violin plot showing the probability distribution of the ratio of relative wind speed and absolute wind speed in the TCs in the AW case. Ratios >1 indicate the relative wind speed exceeds the absolute wind speed, while ratios <1 indicate the opposite. Data shown here are grid points located within a 250 km radius from the TC center prior to landfall or dissipation, as shown in Fig. 2. The width of each violin reflects the kernel density estimation of the distribution. Black and red lines represent median and mean of this ratio.

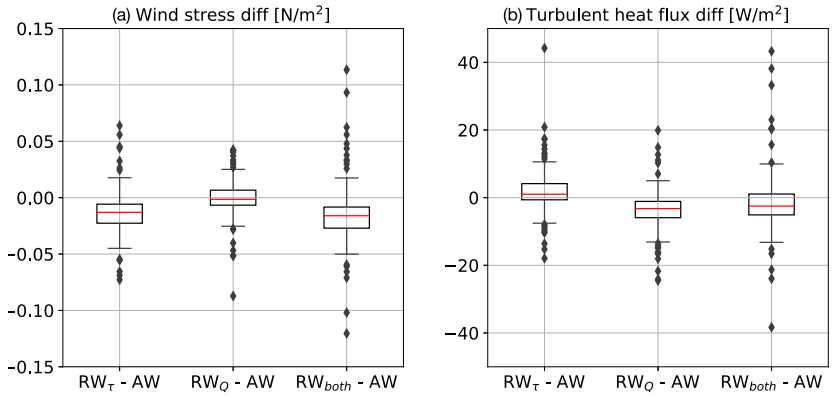

Fig. 4 | Changes in air–sea momentum and turbulent heat fluxes under TCs. Box plots showing the differences of (**a**) wind stress and (**b**) upward turbulent (latent plus sensible) heat flux between experimental cases, calculated within a 250 km radius from the TC center with 6-hourly simulation data, during the period shown in Fig. 2. Box plots illustrate the median differences, represented by red lines, and the interquartile ranges (IQR), depicted as boxes. The whiskers indicate the range of differences, excluding outliers. Outliers are represented by black diamonds.

Responses to current–wind interaction

While the previous subsection examined the surface currents and relative wind in the control case (AW), this subsection compares the four experimental cases listed in Table 1 to evaluate the effects of different current–wind interaction settings. We composited the mean wind stress and turbulent heat flux within the 250 km radius from TC centers from 6 hourly output and compared those fluxes. Both wind stress and turbulent heat flux decreased when the relative wind was used instead of the absolute wind (Fig. 4). For the wind stress difference distribution, the first box plot ($RW_\tau - AW$) and the third box plot ($RW_{both} - AW$) showed negative values in >75% of the total time steps for all TCs, indicating that including surface currents reduces the air–sea momentum flux (Fig. 4a). The median of turbulent heat flux difference was negative in the second box plot ($RW_Q - AW$) and the third box plot, suggesting a reduction in turbulent heat flux due to surface currents (Fig. 4b). Figure S4 represents the mean differences for each TC, and eight TCs (Nepartak, Meranti, Malakas, Megi, Haima, Meari in 2016; Jebi and Kong-Rey in 2018) show decreases in both wind stress (in RW_τ and RW_{both}) and turbulent heat flux (in RW_Q and RW_{both}) compared to the control run (AW). Including surface currents in the flux calculation in these eight TCs led to mean reduction of 2.5 and 1.0% in wind stress and turbulent heat flux, respectively. These results indicate that, despite the extreme wind conditions, surface currents significantly influence both air–sea momentum and turbulent heat exchange.

Since wind stress and heat flux act as the energy sink and source of TCs, respectively, we examined how changes in these fluxes affected TC intensity in the eight selected TCs (Fig. 5). We selected these eight TCs in which both wind stress and turbulent heat flux decreased in the surface current coupling cases compared to the AW. This selection allows for a clear comparison of the individual impacts of reduced wind stress in RW_τ and reduced turbulent heat flux in RW_Q on TC intensity, with the combined effect represented by RW_{both}. We evaluated TC intensity using changes in maximum surface wind speed and minimum sea-level pressure. A surface wind speed ratio >1 indicates a stronger TC when using relative wind, while a negative sea-level pressure difference can be interpreted similarly. For the maximum surface wind speed relative to the AW case, the medians of RW_τ and RW_{both} exceed 1, while that of RW_Q is <1 (Fig. 5(a)). The minimum sea level pressure is lower in RW_τ and higher in RW_Q than AW over more than 75% of time steps during TCs (Fig. 5(b)), representing the strengthening and weakening of TCs, respectively.

Changes in TC intensity for individual TC are provided in Fig. S5. We used the positions of the medians to describe the intensity changes. In the

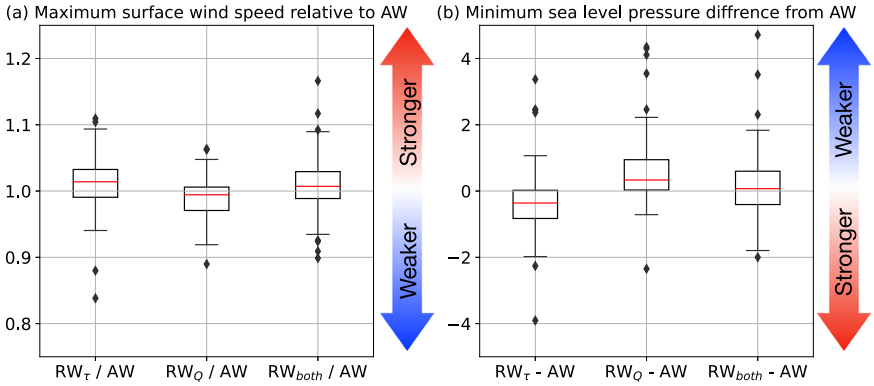

Fig. 5 | Changes in TC intensity. Box plots showing the changes in TC intensity with (**a**) maximum surface wind speed (WS) relative to control case (AW) and (**b**) minimum sea level pressure (SLP) difference from control case with 6-h simulation data.

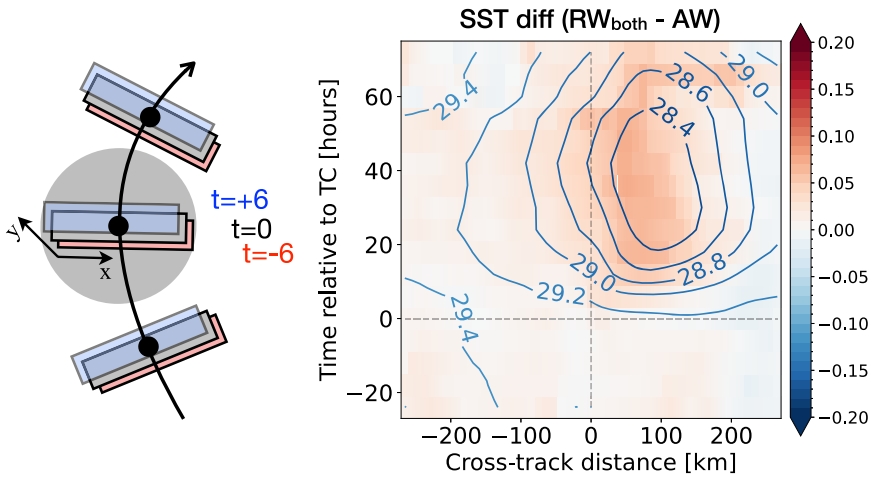

Fig. 6 | SST changes before and after TC passage. Composite mean SST relative to the TC center (*x*-axis) and time from TC passage (*y*-axis), averaged over grid points located within 250 km perpendicular to the TC track. The contour lines indicate the mean SST in the AW case. The shading represents the difference in SST (RW$_{\mathrm{both}}$ − AW).

RW$_\tau$ case, reduced wind stress decreased energy dissipation, which intensified in 6 out of 8 TCs (left group in Fig. S5). In contrast, the RW$_Q$ case showed that reduced turbulent heat flux weakened the energy supply, and 7 out of 8 TCs exhibited median values indicating weakening (middle group in Fig. S5). The theoretical framework predicts that RW$_{\mathrm{both}}$ would have a net intensifying effect, albeit weaker than RW$_\tau$. In the simulation output, the RW$_{\mathrm{both}}$ showed a weaker intensifying effect than RW$_\tau$ or even a weakening effect (right group in Fig. S5).

It is noted that maximum surface wind speed and minimum sea-level pressure sometimes suggest inconsistent results regarding the TC intensities. For example, in the right groups Fig. S5(a), 7 of 8 TCs showed a surface wind speed ratio >1 in RW$_{\mathrm{both}}$, but only one TC (2018 Kong-Rey) had a negative sea-level pressure difference (Fig. S5(b)). The inconsistent intensification observed in RW$_{\mathrm{both}}$ may stem from the differing characteristics of the two intensity metrics: maximum surface wind speed represents a localized extreme, whereas minimum sea-level pressure reflects the broader structural state of the storm. Furthermore, previous studies have shown that the wind-pressure relationship is not strictly linear, but modulated by factors such as storm size, translational speed, and environmental thermodynamic conditions[38,39]. Consequently, wind and pressure may exhibit distinct responses to current-wind interaction. The minimum sea-level pressure difference suggests that, when both wind stress and turbulent heat flux responses are combined, the effects of the source and sink terms of TC energy—outlined in the Theoretical framework — may compensate for each other.

To assess the magnitude of the intensity change relative to the intrinsic TC growth, we first quantified the net sea-level pressure depression for each TC in the control case (AW), defined as the difference between the initial sea-level pressure and the minimum sea-level pressure during the simulation. For each experimental cases, the difference in minimum sea-level pressure from AW was then calculated and normalized by the corresponding net sea-level pressure depression of that TC, expressed as a percentage. This metric indicates how large the changes in intensity was compared to the total growth of the TC. The average relative changes observed across all time steps and TCs were +1.3% for RW$_\tau$, −1.9% for RW$_Q$, and −0.4% for RW$_{\mathrm{both}}$. The largest relative changes observed across all time steps and TCs were +11.1% for RW$_\tau$, −13.7% for RW$_Q$, and +11.1% for RW$_{\mathrm{both}}$. To check whether changes were larger than the internal variability of model, we created and compared three ensemble members for the case of Typhoon Kong-rey. These members were perturbed with in initial SST condition of an absolute value <0.01° C at the point of divergence for each experimental case. In the ensemble members, the changes were within −6.6% to +4.9%. Notably, these values represent the greatest difference at any point in the simulation period, rather than differences at the time of peak TC intensity.

The compensating effect does not imply that RW$_{\mathrm{both}}$ remains unchanged. When we examined oceanic response, we observed clear differences. To assess how current–wind interaction influences this response, we compared SST cooling, a well-known oceanic response to TCs. As shown in the contours in Fig. 6, TCs exhibited post-TC SST cooling of 1 ° C on average (contours). The shading represents the SST difference between RW$_{\mathrm{both}}$ and AW, revealing warmer SST in RW$_{\mathrm{both}}$—indicating less cooling. There are multiple drivers that contribute to the cold wake, such as TC intensity, size, translation speed, and upper ocean stratification[16,40]. Here, weaker SST cooling in RW$_{\mathrm{both}}$ is likely due to reduced upper-ocean mixing with weaker wind stress compared to AW (Fig. 4). It is worth noting that 2018 Kong-Rey showed weaker SST

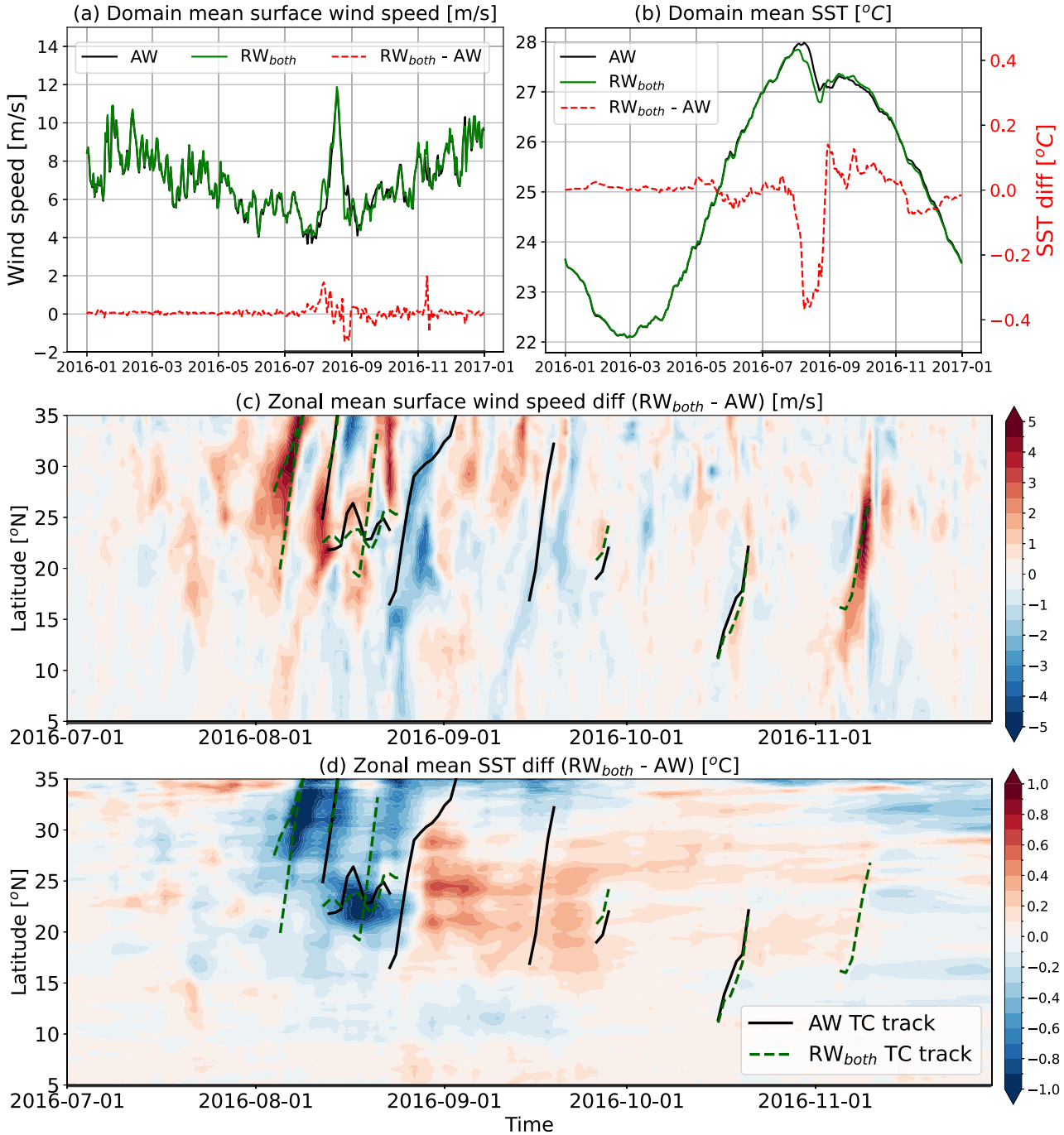

Fig. 7 | Changes in wind speeds and SST in the 12-month simulation. a, **b** Time series of the mean surface wind speed and SST in the TC genesis region (5° N –35 ° N, 117° E– 157 ° E) from a 12 month simulation with the difference of each variable between RW_{both} and AW. **c**, **d** show an enlarged view of the period from July onward, presenting time-latitude plots of zonal-mean surface wind speed and SST differences between RW_{both} and AW. Black solid lines indicate the latitudes of TCs in the AW simulation, while green dashed lines indicate those in the RW_{both} simulation.

cooling in RW_{both} (Fig. S6) despite having a stronger TC compared to AW (Fig. S5). SST is one of the dominant factors influencing TC activity. This oceanic response, in turn, might affect the generation and translation of the subsequent TCs.

To evaluate whether these effects extend beyond individual TCs, we ran a 12 month simulation for the year 2016 under both AW and RW_{both} experimental cases. In the TC genesis region (5 ° N – 35 ° N), we compared the mean surface wind speed and SST (Fig. 7a, b). Differences between the two simulations became pronounced during the TC season, which started in July. Analysis of zonal mean wind speed, SST, and detected TCs showed that certain TCs developed only in one simulation (Lines in Fig. 7c, d). TC genesis differed from the beginning of the period: two TCs developed only in RW_{both} in early August, leading to a local increase in surface wind speed and significant SST cooling. This resulted in a positive zonal mean surface wind speed difference and a negative SST difference up to 1 ° C (Shading in Fig. 7c, d). Additional non-overlapping TCs also emerged later in the simulation. These results indicate that current–wind interaction affects not only the intensity of individual TCs but also modulates large-scale atmospheric and oceanic states and TC activity.

Discussion

Under the TC, strong, wind-aligned surface currents develop, leading to a reduction in air–sea flux via current–wind interaction. The reduced wind stress, which is associated with the TC's energy sink, contributes to its intensification, whereas the reduced enthalpy flux or turbulent (latent plus sensible) heat flux weakens the TC. As presented in the Theoretical framework based on changes in the PI formula and the energy trajectory of TCs, the numerical experiments confirmed that TC intensity was modified generally consistent with our expectation.

In addition to the direct effects of current–wind interactions, SST may also play a role in modulating TC intensity. As shown in Fig. 6 and Fig. S6, SST differences between RW_{both} and AW are evident, and similar analyses for RW_τ and RW_Q are presented in Figs. S7 and S8. In RW_τ, post-TC SST cooling is weaker than in AW, likely due to reduced wind stress, similar to what is observed in RW_{both}. The magnitude of the SST difference is smaller than in RW_{both}, possibly because the intensified TC in RW_τ partially compensates for the weakened cold wake. These weaker cold wake—resulting in warmer SSTs—could, in turn, indirectly contribute to TC intensification in both RW_{both} and RW_τ. In contrast, RW_Q shows little change in SST cooling, as the cold wake is primarily a wind-driven process and less sensitive to changes in turbulent heat flux[16,41,42].

However, some TCs did not exhibit weakening in RW_τ and strengthening in RW_Q (Fig. S5). These discrepancies can be explained as follows. The TCs that responded in line with the theoretical framework (Nepartak, Meranti, Malakas, Megi in 2016; Jebi and Kong-Rey in 2018) showed the average wind–current angles in the right semicircle of within 35°. In contrast, for TCs (b), (i) and (j) in Fig. S2, the average angles are above 40°, meaning the current–wind interaction is less significant. This discrepancy in wind–current angles might be influenced by several factors, such as mesoscale eddies, western boundary currents, or the mixed layer depth. Further studies are needed to ascertain the underlying mechanisms.

Another explanation lies in the way TC intensity responds to current–wind interactions. In a direct response, these interactions immediately alter TC intensity as mentioned. Alternatively, a feedback response occurs when an initial intensification or weakening of the TC caused by changes in air–sea fluxes changes surface wind speed, which then affects momentum and enthalpy fluxes. Additionally, there can be an indirect response, where current–wind interactions modify the oceanic background state, subsequently influencing TC intensity. This mechanism could account for the complex intensity changes shown in Fig. 5.

Despite these complexities, our findings demonstrate that current–wind interactions remain effective even under extreme wind conditions. Moreover, they modulate both TC intensity and oceanic responses, suggesting a novel TC-ocean interaction through surface currents. Given that such interactions can influence not only the intensity of individual TCs but also TC genesis, affecting seasonal wind speed and SST patterns. Incorporating them into coupled modeling systems may therefore improve TC forecasts and climate projections.

Methods

Modified potential intensity

In the PI theory, entropy gain, defined as the sum of the enthalpy flux and mechanical heating multiplied by the thermal efficiency, is assumed to be equal to entropy loss through frictional dissipation[29].

$$\frac{T_s-T_{out}}{T_s}\{C_h|\mathbf{V}_{atm}|(h^*-h)+\mathbf{V}_{atm}\cdot C_D|\mathbf{V}_{atm}|\mathbf{V}_{atm}\} = \mathbf{V}_{atm}\cdot C_D|\mathbf{V}_{atm}|\mathbf{V}_{atm}, \tag{3}$$

where T_s is the surface temperature, T_{out} is the temperature at the outflow layer, C_h and C_D are the exchange coefficients for enthalpy and momentum, respectively, $\mathbf{V}_{atm}$ is the surface wind vector at the radius of maximum winds, h^* is the saturation enthalpy of the sea surface, and h is the enthalpy of the atmosphere. In Eq. (3), the first term within the curly brackets on the left-hand side represents the enthalpy flux, while the second term on the left-hand side and the one on the right-hand side correspond to the sink of momentum. From this equation, PI using absolute surface wind (AW) can be derived as[28,29]

$$PI(AW) = |\mathbf{V}_{atm}|^2 = \frac{T_s-T_{out}}{T_{out}}\frac{C_h}{C_D}(h^*-h). \tag{4}$$

To account for the change of enthalpy flux and wind stress considering surface currents, we modify the PI to account for the relative wind vector. By replacing $\mathbf{V}_{atm}$, which is used in enthalpy flux and wind stress, with the wind vector relative to the ocean current, $\mathbf{V}_{atm}-\mathbf{V}_{ocn}$, Eq. (3) becomes

$$\frac{T_s-T_{out}}{T_s}\{C_h|\mathbf{V}_{atm}-\mathbf{V}_{ocn}|(h^*-h)+\mathbf{V}_{atm}\cdot C_D|\mathbf{V}_{atm}-\mathbf{V}_{ocn}|(\mathbf{V}_{atm}-\mathbf{V}_{ocn})\} = \mathbf{V}_{atm}\cdot C_D|\mathbf{V}_{atm}-\mathbf{V}_{ocn}|(\mathbf{V}_{atm}-\mathbf{V}_{ocn}). \tag{5}$$

If we introduce α and θ as the ratio of the relative wind speed to the absolute wind speed and the angle between these two wind vectors, respectively,

$$|\mathbf{V}_{atm}-\mathbf{V}_{ocn}| = \alpha|\mathbf{V}_{atm}| \tag{6}$$

$$\begin{aligned}\mathbf{V}_{atm}\cdot(\mathbf{V}_{atm}-\mathbf{V}_{ocn}) &= |\mathbf{V}_{atm}||\mathbf{V}_{atm}-\mathbf{V}_{ocn}|\cos\theta\\ &= \alpha\cos\theta|\mathbf{V}_{atm}|^2.\end{aligned} \tag{7}$$

Then (5) can be expressed using $\mathbf{V}_{atm}$, α, and θ

$$\frac{T_s-T_{out}}{T_s}\left\{\alpha C_h|\mathbf{V}_{atm}|(h^*-h)+\alpha^2 C_D\cos\theta|\mathbf{V}_{atm}|^3\right\} = \alpha^2 C_D\cos\theta|\mathbf{V}_{atm}|^3, \tag{8}$$

which yields

$$PI(RW_{both}) = |\mathbf{V}_{atm}|^2 = \frac{1}{\alpha\cos\theta}\frac{T_s-T_{out}}{T_{out}}\frac{C_h}{C_D}(h^*-h) = \frac{1}{\alpha\cos\theta}PI(AW). \tag{9}$$

where RW_{both} indicates this PI is derived using the relative wind in both enthalpy and momentum flux. If we incorporate the surface current vector into the terms related to either enthalpy flux (RW_Q) or momentum flux (RW_τ) alone, the potential intensities are modified as

$$PI(RW_Q) = |\mathbf{V}_{atm}|^2 = \alpha\frac{T_s-T_{out}}{T_{out}}\frac{C_h}{C_D}(h^*-h) = \alpha PI(AW), \tag{10}$$

and

$$PI(RW_\tau) = |\mathbf{V}_{atm}|^2 = \frac{1}{\alpha^2\cos\theta}\frac{T_s-T_{out}}{T_{out}}\frac{C_h}{C_D}(h^*-h) = \frac{1}{\alpha^2\cos\theta}PI(AW), \tag{11}$$

respectively. The formulation of enthalpy flux and momentum flux used here is described in Table 1.

Growth rate of the TC wind speed

In non-steady conditions, the time rate of change of TC kinetic energy can be expressed by the sum of the actual generation rate of mechanical energy and the viscous dissipation rate[36]:

$$\frac{d}{dt}\left(\frac{\rho A_e H|\mathbf{V}_{atm}|^2}{2}\right) = \rho A_e C_h k(h^*-h)\left(1-\frac{T_{out}}{T_s}\right)|\mathbf{V}_{atm}| - \rho A_e C_D\frac{T_{out}}{T_s}|\mathbf{V}_{atm}|^3 \tag{12}$$

where ρ is the air density near the surface, A_e is the effective surface area covered by a TC, $H=\frac{1}{\rho}\int\rho(z)dz$ is the density scale height of the

atmosphere and k is the relative efficiency factor ($0 \le k \le 1$). Rearranging this equation after considering surface currents yields the growth rate of the TC wind speed.

$$\frac{d|\mathbf{V}_{\mathrm{atm}}|}{dt} = \frac{1}{H|\mathbf{V}_{\mathrm{atm}}|}\left(k\left(1-\frac{T_{\mathrm{out}}}{T_s}\right)C_h(h^*-h)|\mathbf{V}_{\mathrm{atm}}-\mathbf{V}_{\mathrm{ocn}}| - C_D\frac{T_{\mathrm{out}}}{T_s}|\mathbf{V}_{\mathrm{atm}}-\mathbf{V}_{\mathrm{ocn}}|^2|\mathbf{V}_{\mathrm{atm}}|\right) \quad (13)$$

where the first term in the parentheses corresponds to the energy source term from the upward enthalpy flux, while the second term denotes the sink term from viscous dissipation. If the source exceeds the sink, the TC wind speed intensifies; otherwise, it weakens. To visualize this, we prescribed time-varying surface current speed that increased from 0.3 m/s to 1.5 m/s and then decreased to 0.5 m/s (Fig. S9a), assuming they are aligned with the surface wind. The SST and relative humidity were also varied, initially remaining constant at 302 K and 0.8 before decreasing to 293 K and increasing to 0.9, respectively (Fig. S9b, c). We also assume constant coupling coefficients $C_h = 1.15 \times 10^{-3}$ and $C_D = 1.3 \times 10^{-3}$ [43], typical values of $T_{out} = 205$ K, H = 7500 m, and the enthalpy difference following[36] and references therein.

Description of model and experiments

We use the coupled atmosphere–ocean model known as the Scripps–KAUST Regional Integrated Prediction System (SKRIPS) v1.2[44]. SKRIPS integrates the atmospheric component Weather Research and Forecasting (WRF,[45]) and the oceanic component MIT general circulation model (MITgcm,[46]) combined through the Earth System Modeling Framework (ESMF) coupler[47]. In the coupled system, 10-m wind, air–sea heat fluxes, moisture flux, precipitation and surface pressure are transferred from the atmosphere model to the ocean model, while surface current and SST are transferred from the ocean model to the atmosphere model. The WRF uses WSM6 microphysics[48], New Tiedtke cumulus scheme, Mellor-Yamada-Nakanishi-Niino (MYNN) surface layer and planetary boundary layer[49,50], and the Rapid Radiative Transfer Model for GCMs (RRTMG) longwave and shortwave[51] as physical schemes. Both models have a horizontal resolution of 0.1°, with a time step of 30 s for WRF and 180 s for MITgcm. The coupling frequency was set to 180 s.

We designed experiments to examine the isolated effects of momentum flux and enthalpy flux change on TC intensities (Table 1). In the control simulation, air–sea fluxes are calculated using the absolute wind in all cases. In the RW_τ experiment, the momentum flux is computed using the relative wind, while in the RW_Q experiment, the enthalpy flux is calculated using the relative wind. In the RW_{both} experiment, both fluxes are computed using the relative wind, allowing us to assess the combined effect of these changes.

The model domain covers the western North Pacific, extending from 0 to 51.2° N and from 117 to 157° E. The ocean model boundary fields were obtained from Ocean Reanalysis System 5 (ORAS5)[52], and initial conditions were taken from spin-up simulation initialized on May 1 of 2016, 2017, and 2018 using ORAS5 fields. Since ORAS5 has a resolution of 0.25° while the SKRIPS model operates at 0.1°, the spin-up simulation generate more realistic dynamics and stronger currents. The spin-up simulation outputs were used as the initial condition after the domain-mean surface kinetic energy saturation. The atmosphere model was initialized with the European Centre for Medium-Range Weather Forecasts Reanalysis v5 (ERA5)[53] at the TC genesis time. To allow the atmospheric model to adjust the initial and boundary conditions, the coupled system was run for 12–24 h before diverging into different experimental cases. Since the initial development varied among TCs, a 12 h spin-up was used for rapidly intensifying cases.

We simulated twelve TCs that occurred in the western North Pacific from 2016−2018. Those twelve TCs were selected based on the following criteria: (1) having a typhoon stage lasting >2 days according to the Joint Typhoon Warning Center (JTWC) best track data, (2) maintaining typhoon intensity for >2 days without land interaction, and (3) remaining within the model domain from the time they reached severe tropical storm status (maximum wind speed >48 knots) until landfall or dissipation. Additionally, we only included TCs for which ocean initial conditions were available from spin-up simulations.

The methods used to detect and track TCs were adapted from previous studies[54,55]. The criteria used for TC tracking in our simulations are as follows: a local minimum in surface pressure, a maximum 10-m wind speed exceeding 16 m/s, a maximum 850 hPa vorticity >4.5×10^{-5} s^{-1} and a sum of temperature anomaly at 850 hPa, 500 hPa, and 200 hPa > 1.5 K. The TC tracks simulated in each case are shown in Fig. 2. For the analysis, we only considered the period before landfall to focus on the surface current effects. The period, maximum surface wind speed, and minimum sea level pressure are summarized in Table S1.

Drag coefficient (C_D) representation under high winds could affect the TC intensity and structure simulation[56] and the ratio of the exchange coefficients (C_h/C_D) is important for the TC intensity. In MYNN surface layer scheme, C_h/C_D remains unchanged when the wind speed exceeds 25 m/s[57]. The surface exchange coefficients are expressed as: $C_D = \frac{k^2}{[\ln(\frac{z_1+z_0}{z_0})-\psi_M(\frac{z_1+z_0}{L})+\psi_M(\frac{z_0}{L})]^2}$, $C_h = \frac{k^2}{[\ln(\frac{z_1+z_0}{z_0})-\psi_M(\frac{z_1+z_0}{L})+\psi_M(\frac{z_0}{L})][\ln(\frac{z_1+z_0}{z_h})-\psi_H(\frac{z_1+z_0}{L})+\psi_H(\frac{z_h}{L})]}$, where k is the von Karman constant (= 0.4), z_0 is the surface aerodynamic roughness length, z_h is the scalar roughness length for heat and moisture, L is the Obukhov length, z_1 is the height of the first model half-level, and $\psi_{M,H}$ is a stability function. Although the MYNN scheme computes surface exchange coefficients and the roughness lengths for heat and moisture separately, they are identical in most configurations[58]. Therefore, we adopted the enthalpy exchange coefficient form described above. The roughness lengths are specified by the COARE 3.0 algorithm[43]. The aerodynamic roughness length for COARE 3.0 is a function of u_* and the 10 m wind speed, U10, with a variable Charnock parameter. When calculating the Charnock parameter, U10 is bounded between 10 and 18 m/s, and there are lower and upper bounds for roughness length. Therefore, the exchange coefficients remain constant outside of the bound. According to the available observational data, C_h and C_D increase with wind speed and then level off, while C_D even decreases in strong wind[59–63]. However, there is still uncertainty about the behavior of exchange coefficients[64,65]. We performed additional theoretical sensitivity tests in varying C_D and C_h. Although the absolute value of the source and sink term of TC energy budget are modified, the current–wind interaction continues to weaken the TC in the RW_Q and strengthen it in the RW_τ and RW_{both}.

Data availability

The Scripps-KAUST Regional Integrated Prediction System (SKRIPS) v1.2 (Sun et al. 2019) is available in the github repository, https://github.com/iurnus/scripps_kaust_model/releases/tag/v1.2. The Joint Typhoon Warning Center (JTWC) best track data is obtained from https://www.metoc.navy.mil/jtwc/jtwc.html?best-tracks.

Code availability

The analytical code employed for the results in this paper is not publicly available but may be made available to qualified researchers on reasonable request from the corresponding author.

Received: 29 August 2025; Accepted: 26 December 2025;
Published online: 16 January 2026

References

1. Cronin, M. F. et al. Air-sea fluxes with a focus on heat and momentum. *Front. Marine Sci.* https://doi.org/10.3389/fmars.2019.00430 (2019).
2. Smith, S. D., Fairall, C. W., Geernaert, G. L. & Hasse, L. Air-sea fluxes: 25 years of progress. *Bound. Layer. Meteorol.* **78**, 247–290 (1996).
3. Bourassa, M. A. et al. High-latitude ocean and sea ice surface fluxes: challenges for climate research. *Bull. Am. Meteorol. Soc.* **94**, 403–423 (2013).
4. Yu, L. Global air-sea fluxes of heat, fresh water, and momentum: energy budget closure and unanswered questions. *Annu. Rev. Mar. Sci.* **11**, 227–248 (2019).

5. Renault, L., Molemaker, M. J., Gula, J., Masson, S. & McWilliams, J. C. Control and stabilization of the gulf stream by oceanic current interaction with the atmosphere. *J. Phys. Oceanogr.* **46**, 3439–3453 (2016).
6. Renault, L., McWilliams, J. C. & Penven, P. Modulation of the agulhas current retroflection and leakage by oceanic current interaction with the atmosphere in coupled simulations. *J. Phys. Oceanogr.* **47**, 2077–2100 (2017).
7. Renault, L., McWilliams, J. C. & Masson, S. Satellite observations of imprint of oceanic current on wind stress by air-sea coupling. *Sci. Rep.* **7**, 17747 (2017).
8. Seo, H., Miller, A. J. & Norris, J. R. Eddy-wind interaction in the california current system: dynamics and impacts. *J. Phys. Oceanogr.* **46**, 439–459 (2016).
9. Seo, H., Subramanian, A. C., Song, H. & Chowdary, J. S. Coupled effects of ocean current on wind stress in the Bay of Bengal: Eddy energetics and upper ocean stratification. *Deep Sea Res. Part II: Topical Stud. Oceanogr.* **168**, 104617 (2019).
10. Song, H., Marshall, J., McGillicuddy, D. J. & Seo, H. Impact of current-wind interaction on vertical processes in the Southern Ocean. *J. Geophys. Res. Oceans* **125**, e2020JC016046 (2020).
11. Jullien, S. et al. Impact of ocean-atmosphere current feedback on ocean mesoscale activity: regional variations and sensitivity to model resolution. *J. Clim.* **33**, 2585–2602 (2020).
12. Larrañaga, M., Renault, L. & Jouanno, J. Partial control of the gulf of mexico dynamics by the current feedback to the atmosphere. *J. Phys. Oceanogr.* **52**, 2515–2530 (2022).
13. Cho, A. et al. Dynamic and thermodynamic coupling between the atmosphere and ocean near the Kuroshio current and extension system. *Ocean Model.* **194**, 102496 (2025).
14. Emanuel, K. An air-sea interaction theory for tropical cyclones. Part I: steady-state maintenance. *J. Atmos. Sci.* **43**, 585–605 (1986).
15. Scoccimarro, E. et al. Effects of Tropical Cyclones on Ocean Heat Transport in a High-Resolution Coupled General Circulation Model. *J. Clim.* **24**, 4368–4384 (2011).
16. Price, J. Upper ocean response to a hurricane. *J. Phys. Oceanogr.* **11**, 153–175 (1981).
17. Wang, Y. & Wu, C.-C. Current understanding of tropical cyclone structure and intensity changes ? a review. *Meteorol. Atmos. Phys.* **87**, 257–278 (2004).
18. Zhu, T. & Zhang, D.-L. The impact of the strom-induced sst cooling on hurricane intensity. *Adv. Atmos. Sci.* **23**, 14–22 (2006).
19. Hart, R. E., Maue, R. N. & Watson, M. C. Estimating local memory of tropical cyclones through MPI anomaly evolution. *Monthly Weather Rev.* **135**, 3990–4005 (2007).
20. Bender, M. A. & Ginis, I. Real-case simulations of hurricane-ocean interaction using a high-resolution coupled model: effects on hurricane intensity. *Monthly Weather Rev.* **128**, 917–946 (2000).
21. Hlywiak, J. & Nolan, D. S. The influence of oceanic barrier layers on tropical cyclone intensity as determined through idealized, coupled numerical simulations. *J. Phys. Oceanogr.* **49**, 1723–1745 (2019).
22. Moon, I.-J., Ginis, I. & Hara, T. Effect of surface waves on air-sea momentum exchange. Part ii: behavior of drag coefficient under tropical cyclones. *J. Atmos. Sci.* **61**, 2334–2348 (2004).
23. Moon, I.-J., Ginis, I., Hara, T. & Thomas, B. A physics-based parameterization of air-sea momentum flux at high wind speeds and its impact on hurricane intensity predictions. *Monthly Weather Rev.* **135**, 2869–2878 (2007).
24. Zhao, B. et al. A numerical study of tropical cyclone and ocean responses to air-sea momentum flux at high winds. *J. Geophys. Res. Oceans* **129**, e2024JC020956 (2024).
25. Palmén, E. H. On the formation and structure of tropical cyclones. *Geophysica* **3**, 26–38 (1948).
26. Peduzzi, P. et al. Global trends in tropical cyclone risk. *Nat. Clim. Change* **2**, 289–294 (2012).
27. Holland, G. J. The maximum potential intensity of tropical cyclones. *J. Atmos. Sci.* **54**, 2519–2541 (1997).
28. Bister, M. & Emanuel, K. A. Dissipative heating and hurricane intensity. *Meteorol. Atmos. Phys.* **65**, 233–240 (1998).
29. Rousseau-Rizzi, R. & Emanuel, K. An evaluation of hurricane superintensity in axisymmetric numerical models. *J. Atmos. Sci.* **76**, 1697–1708 (2019).
30. Lin, I. et al. An ocean coupling potential intensity index for tropical cyclones. *Geophys. Res. Lett.* **40**, 1878–1882 (2013).
31. Balaguru, K. et al. Dynamic Potential Intensity: an improved representation of the ocean's impact on tropical cyclones. *Geophys. Res. Lett.* **42**, 6739–6746 (2015).
32. Kwon, Y. C. & Kim, T. Impact of air-sea exchange coefficients on the structure and intensity of tropical cyclones. *Terrestrial Atmos. Ocean. Sci.* **28**, 345–356 (2017).
33. Lee, W., Kim, S.-H., Moon, I.-J., Bell, M. M. & Ginis, I. New parameterization of air-sea exchange coefficients and its impact on intensity prediction under major tropical cyclones. *Front. Mar. Sci.* **9**, 1046511 (2022).
34. Zhang, H., He, H., Zhang, W.-Z. & Tian, D. Upper ocean response to tropical cyclones: a review. *Geosci. Lett.* **8**, 1 (2021).
35. Fan, S. et al. Observed ocean surface winds and mixed layer currents under tropical cyclones: asymmetric characteristics. *J. Geophys. Res.: Oceans* **127**, e2021JC017991 (2022).
36. Ozawa, H. & Shimokawa, S. Thermodynamics of a tropical cyclone: generation and dissipation of mechanical energy in a self-driven convection system. *Tellus A: Dyn. Meteorol. Oceanogr.* **67**, 24216 (2015).
37. Aguiar, W. et al. Antarctic Dense Water Formation Sensitivity to Ocean Surface Cell Thickness. *J. Adv. Model. Earth Syst.* **17**, e2024MS004913 (2025).
38. Knaff, J. A. & Zehr, R. M. Reexamination of tropical cyclone wind-pressure relationships. *Weather Forecast.* **22**, 71–88 (2007).
39. Holland, G. A revised hurricane pressure-wind model. *Monthly Weather Rev.* **136**, 3432–3445 (2008).
40. Looney, L. B. & Foltz, G. R. Drivers of tropical cyclone—induced ocean surface cooling. *J. Geophys. Res. Oceans* **130**, e2024JC021610 (2025).
41. Huang, P., Sanford, T. B. & Imberger, J. Heat and turbulent kinetic energy budgets for surface layer cooling induced by the passage of Hurricane Frances (2004). *J. Geophys. Res. Oceans* **114**, 2009JC005603 (2009).
42. Vincent, E. M. et al. Processes setting the characteristics of sea surface cooling induced by tropical cyclones. *J. Geophys. Res. Oceans* **117**, 2011JC007396 (2012).
43. Fairall, C. W., Bradley, E. F., Hare, J. E., Grachev, A. A. & Edson, J. B. Bulk parameterization of air-sea fluxes: updates and verification for the COARE algorithm. *J. Clim.* **16**, 571–591 (2003).
44. Sun, R. et al. SKRIPS v1.0: a regional coupled ocean-atmosphere modeling framework (MITgcm-WRF) using ESMF/NUOPC, description and preliminary results for the Red Sea. *Geosci. Model Dev.* **12**, 4221–4244 (2019).
45. Skamarock, C. et al. *A Description of the Advanced Research WRF Model Version 4.1*. https://opensky.ucar.edu/challenge?destination=/islandora/object/technotes%253A576 (2019).
46. Marshall, J., Adcroft, A., Hill, C., Perelman, L. & Heisey, C. A finite-volume, incompressible Navier Stokes model for studies of the ocean on parallel computers. *J. Geophys. Res. Oceans* **102**, 5753–5766 (1997).
47. Hill, C., DeLuca, C., Balaji, Suarez, M. & Da Silva, A. The architecture of the earth system modeling framework. *Comput. Sci. Eng.* **6**, 18–28 (2004).
48. Hong, S.-Y. & Lim, J.-O. J. The WRF single-moment 6-class microphysics scheme (WSM6). *Asia-Pac. J. Atmos. Sci.* **42**, 129–151 (2006).

49. Nakanishi, M. & Niino, H. An improved mellor-yamada level-3 model with condensation physics: its design and verification. *Bound.-Layer. Meteorol.* **112**, 1–31 (2004).
50. Nakanishi, M. & Niino, H. Development of an improved turbulence closure model for the atmospheric boundary layer. *J. Meteorol. Soc. Jpn. Ser. II* **87**, 895–912 (2009).
51. Iacono, M. J. et al. Radiative forcing by long-lived greenhouse gases: Calculations with the AER radiative transfer models. *J. Geophys. Res. Atmos.* https://doi.org/10.1029/2008JD009944 (2008).
52. Zuo, H., Balmaseda, M. A., Tietsche, S., Mogensen, K. & Mayer, M. The ECMWF operational ensemble reanalysis–analysis system for ocean and sea ice: a description of the system and assessment. *Ocean Sci.* **15**, 779–808 (2019).
53. Hersbach, H. et al. The ERA5 global reanalysis. *Q. J. R. Meteorol. Soc.* **146**, 1999–2049 (2020).
54. Cha, D.-H., Jin, C.-S., Lee, D.-K. & Kuo, Y.-H. Impact of intermittent spectral nudging on regional climate simulation using Weather Research and Forecasting model. *J. Geophys. Res.* https://doi.org/10.1029/2010JD015069 (2011).
55. Kim, T. et al. Characteristics of tropical cyclones over the western North Pacific related to extreme ENSO and a climate regime shift in sub-seasonal forecasting with GloSea5. *Clim. Dyn.* **61**, 2637–2653 (2023).
56. Wang, H. et al. The wind-dependent surface drag coefficient contributes to the secondary eyewall formation in tropical cyclones: a case study of typhoon gaemi (2024). *Geophys. Res. Lett.* **52**, e2025GL117521 (2025).
57. Hoang, T.-H., Huang, C.-Y. & Nguyen, T.-C. Effects of surface layer physics schemes on the simulated intensity and structure of typhoon rai (2021). *Atmosphere* **15**, 1140 (2024).
58. Olson, J. B. et al. *A Description of the MYNN Surface-Layer Scheme.* https://repository.library.noaa.gov/view/noaa/30605 (2021).
59. Powell, M. D., Vickery, P. J. & Reinhold, T. A. Reduced drag coefficient for high wind speeds in tropical cyclones. *Nature* **422**, 279–283 (2003).
60. Black, P. G. et al. Air-sea exchange in hurricanes: synthesis of observations from the coupled boundary layer air-sea transfer experiment. *Bull. Am. Meteorol. Soc.* **88**, 357–374 (2007).
61. Bell, M. M., Montgomery, M. T. & Emanuel, K. A. Air-sea enthalpy and momentum exchange at major hurricane wind speeds observed during CBLAST. *J. Atmos. Sci.* **69**, 3197–3222 (2012).
62. Shimura, T., Mori, N. & Miyashita, T. Footprint of the air-sea momentum transfer saturation observed by ocean wave buoy network in extreme tropical cyclones. *Coast. Eng.* **191**, 104537 (2024).
63. Davis, J. R. et al. Ocean Surface Wave Slopes and Wind-Wave Alignment Observed in Hurricane Idalia. *J. Geophys. Res. Oceans* **130**, e2024JC021814 (2025).
64. Andreas, E. L. Fallacies of the enthalpy transfer coefficient over the ocean in high winds. *J. Atmos. Sci.* **68**, 1435–1445 (2011).
65. Richter, D. H., Wainwright, C., Stern, D. P., Bryan, G. H. & Chavas, D. Potential low bias in high-wind drag coefficient inferred from dropsonde data in hurricanes. *J. Atmos. Sci*. **78**, 7 (2021).

Acknowledgements

This work was supported by the National Research Foundation of Korea (NRF) grant funded by the Korea government (MSIT) (NRF-2022R1A2C1009792), and the Korea Meteorological Administration Research and Development Program under Grant RS-2025-02221669. I.-J. Moon was supported by Korea Institute of Marine Science & Technology Promotion (KIMST) funded by the Ministry of Oceans and Fisheries, Korea (RS-2025-02217872). H.Seo acknowles support from NSF (OCE-2148120), NASA (80NSSC21K1524), and the Uehiro Center for the Advancement of Oceanography (UC·AO) at the University of Hawai'i at Mānoa. M.R.M. and R.S. were supported by NASA grant 80NSSC23K0979. A.J.M. was partly supported by NSF grant OCE2022868. R.S. gratefully acknowledges the research funding (grant number: OSR-2022-NCM-4829.5) from the Climate Change Center at KAUST (King Abdullah University of Science and Technology).

Author contributions

A.C. conceived the study, performed the numerical simulations, and conducted the analysis. H.Song developed the methodology and contributed to interpreting the results. I.-J.M., H.Seo, R.S., M.R.M., A.C.S., B.D.C., and A.J.M. contributed to discussions and provided guidance. A.C. and H.Song led the manuscript writing, with revisions and editing by I.-J.M., H.Seo, R.S., M.R.M., and B.D.C.

Competing interests

The authors declare no competing interests.

Additional information

Supplementary information The online version contains supplementary material available at https://doi.org/10.1038/s41612-025-01316-1.

Correspondence and requests for materials should be addressed to Hajoon Song.